Science Advances

AAAS

advances.sciencemag.org/cgi/content/full/3/7/e1603150/DC1

Supplementary Materials for

Resolving quanta of collective spin excitations in a millimeter-sized ferromagnet

Dany Lachance-Quirion, Yutaka Tabuchi, Seiichiro Ishino, Atsushi Noguchi, Toyofumi Ishikawa, Rekishu Yamazaki, Yasunobu Nakamura

Published 5 July 2017, *Sci. Adv.* **3**, e1603150 (2017)
DOI: 10.1126/sciadv.1603150

This PDF file includes:

section S1. HAMILTONIAN OF THE HYBRID SYSTEM

The Hamiltonian of the hybrid system is given by

$$\hat{\mathcal{H}}/\hbar = \sum_{p=1}^{\infty} \omega_{10p}^{\text{bare}} \hat{a}_p^\dagger \hat{a}_p + \left(\omega_{\text{q}}^{\text{bare}} - \alpha^{\text{bare}}/2\right) \hat{b}^\dagger \hat{b} + \left(\alpha^{\text{bare}}/2\right) \left(\hat{b}^\dagger \hat{b}\right)^2 + \omega_{\text{m}}^{\text{bare}} \hat{c}^\dagger \hat{c} \tag{S1}$$

$$+ \sum_{p=1}^{\infty} \left(g_{\text{q},10p} \left(\hat{a}_p^\dagger \hat{b} + \hat{a}_p \hat{b}^\dagger \right) + g_{\text{m},10p} \left(\hat{a}_p^\dagger \hat{c} + \hat{a}_p \hat{c}^\dagger \right) \right) \tag{S2}$$

where $\omega_{10p}^{\text{bare}}$ is the bare frequency of the TE_{10p} mode of the cavity, $\omega_{\text{q}}^{\text{bare}} \equiv \omega_{ge}$ and ω_{ef} are, respectively, the bare frequencies of the $|g\rangle \leftrightarrow |e\rangle$ and $|e\rangle \leftrightarrow |f\rangle$ transitions of the transmon qubit, $\alpha^{\text{bare}} \equiv \omega_{ef} - \omega_{ge}$ is the bare anharmonicity of the transmon qubit, $\omega_{\text{m}}^{\text{bare}}$ is the bare magnon frequency, $g_{\text{q},10p}$ is the coupling strength between the TE_{10p} cavity mode and the transmon qubit, and $g_{\text{m},10p}$ is the coupling strength between the TE_{10p} cavity mode and the Kittel mode [16]. In Eq. (S1), $\hat{a}_p^\dagger$ ($\hat{a}_p$), $\hat{b}^\dagger$ ($\hat{b}$), and $\hat{c}^\dagger$ ($\hat{c}$) are the creation (annihilation) operators of, respectively, a photon in the TE_{10p} cavity mode, an excitation in the transmon qubit and a magnon in the Kittel mode. In the Hamiltonian of Eq. (S1), the transmon qubit is considered as an anharmonic oscillator in order to take into account the effect of the $|e\rangle \leftrightarrow |f\rangle$ transition on the values of the calculated parameters, therefore capturing the straddling regime of the qubit-magnon system [21]. Figures S1A and B schematically represent the energy diagram of the hybrid system with the qubit and the Kittel mode in the resonant and dispersive regimes, respectively.

The parameters of the hybrid system in Eq. (S1) are shown in Table S1. We calculate values of the qubit-magnon coupling strength $g_{\text{q-m}}$, the qubit-TE_{103} cavity mode dispersive shift $\chi_{\text{q},103}$, the qubit-magnon dispersive shift $\chi_{\text{q-m}}$, and the magnon Kerr coefficient K_{m} using these parameters and the above Hamiltonian by truncating the sum over the TE_{10p} modes of the cavity to $p = 4$. We consider the TE_{10p} cavity mode number states $|n_{10p} = \{0, 1, 2\}\rangle$, the transmon states $|i = \{g, e, f\}\rangle$, and the Kittel mode magnon number states $|n_{\text{m}} = \{0, 1, 2\}\rangle$. More explicitly, we diagonalize the Hamiltonian and evaluate the parameters with

$$\chi_{\text{q},103} = \frac{1}{2}\left(\omega_{103}^{e} - \omega_{103}^{g}\right)$$

$$\chi_{\text{q-m}} = \frac{1}{2}\left(\omega_{\text{m}}^{e} - \omega_{\text{m}}^{g}\right)$$

$$K_{\text{m}} = 2\omega_{\text{m},0\to1}^{g} - \omega_{\text{m},0\to2}^{g}$$

where $\omega_{103}^{g(e)}$ is the frequency of the TE_{103} cavity mode with the transmon in the ground (excited) state, $\omega_{\text{m}}^{g(e)}$ is the frequency of the Kittel mode with the transmon in the ground (excited) state, and $\omega_{\text{m},0\to n_{\text{m}}}^{g}$ is the transition frequency of the Kittel mode between the magnon vacuum state and the $|n_{\text{m}}\rangle$ magnon number state with the transmon in the ground state, with $\omega_{\text{m}}^{g} \equiv \omega_{\text{m},0\to1}^{g}$, such that for $K_{\text{m}} = 0$, $\omega_{\text{m},0\to n_{\text{m}}}^{g} = n_{\text{m}}\omega_{\text{m}}^{g}$. The qubit-magnon interaction strength $g_{\text{q-m}}$ is simply calculated by half the splitting in the qubit-magnon hybridized energy levels. Figure S1D shows the qubit-magnon dispersive shift $\chi_{\text{q-m}}$ and Fig. S1E shows the magnon Kerr coefficient K_{m}, both calculated as a function of the bare magnon frequency $\omega_{\text{m}}^{\text{bare}}$. Table S2 summarizes the theoretical values of $g_{\text{q-m}}$, $\chi_{\text{q},103}$, $\chi_{\text{q-m}}$, and K_{m}.

As in the main text, the TE_{102} and TE_{103} cavity modes are, from now on, labeled the coupler and probe cavity modes, respectively. Therefore, indices '102' and '103' are replaced by indices 'c' and 'p', respectively.

section S2. CAVITY-MAGNON COUPLING

Data on the avoided crossing between the TE_{102} cavity mode (coupler mode) and the Kittel mode is shown in Fig. S3A. Figure S3B shows the current-dependent dressed cavity frequency with the qubit in the ground state, $\omega_c^g(I)$, extracted from data of Fig. S3A. The dressed cavity frequency is fitted to

$$\omega_c^g(I) = p_1 I + p_2 - \mathrm{sgn}\,(I - I_0)\sqrt{(p_1 I - p_3)^2 + p_4^2} \tag{S3}$$

with the fitting parameters p_1 to p_4 related to the physical quantities by

$$\begin{aligned}
\omega_c^{\mathrm{bare}'} &= p_2 + p_3, \\
\omega_m^{\mathrm{bare}'}(I) &= 2p_1 I + p_2 - p_3, \\
|g_{m-c}| &= p_4, \\
\omega_m^{\mathrm{bare}'}(I_0) &\equiv \omega_c^{\mathrm{bare}'}
\end{aligned}$$

In the above equations, $\omega_c^{\mathrm{bare}'}$ is the frequency of the coupler mode bare of its interaction with the Kittel mode, $\omega_m^{\mathrm{bare}'}$ is the frequency of the Kittel mode bare of its interaction with the coupler mode, g_{m-c} is the coupling strength between the coupler mode and the Kittel mode, and I_0 is the coil current for which $\omega_m^{\mathrm{bare}'} = \omega_c^{\mathrm{bare}'}$. This enables us to determine $\omega_c^{\mathrm{bare}'}/2\pi = 8.456$ GHz.

We furthermore fit the cavity spectrum $\mathrm{Re}(r)$ to

$$\mathrm{Re}(r) = \mathrm{Re}\left(\frac{\omega_r - \omega_c^{\mathrm{bare}'} + \frac{i\left(\kappa_c^{\mathrm{int}} - \kappa_c^{\mathrm{cpl}}\right)}{2} - \frac{|g_{m-c}|^2}{\omega_r - \omega_m^{\mathrm{bare}'}(I) + i\gamma_m/2}}{\omega_r - \omega_c^{\mathrm{bare}'} + \frac{i\kappa_c}{2} - \frac{|g_{m-c}|^2}{\omega_r - \omega_m^{\mathrm{bare}'}(I) + i\gamma_m/2}}\right) \tag{S4}$$

where ω_r is the readout frequency, κ_c^{int} is the internal loss rate of the coupler mode, κ_c^{cpl} is the coupling rate of the input/output port to the coupler mode, $\kappa_c = \kappa_c^{\mathrm{int}} + \kappa_c^{\mathrm{cpl}}$ is the total linewidth of the coupler mode, and γ_m is the magnon linewidth. The coupling rate of an unused port of the cavity is included in the internal loss rate of the cavity. Values of κ_c^{int}, κ_c^{cpl}, and κ_c, given in Table S3, are determined from a measurement of the coupler cavity mode spectrum far from the avoided crossing ($I = -10$ mA) while the value of $\omega_c^{\mathrm{bare}'}$ is fixed by the fit of $\omega_c^g(I)$ to Eq. (S3). The global fitting parameters are γ_m and g_{m-c} while $\omega_m^{\mathrm{bare}'}$ is fitted for each coil current I.

Figure S3C shows spectra fitted to Eq. (S4) for coil currents I near the avoided crossing at $I_0 \approx 5.5$ mA. We find $g_{m-c}/2\pi = 22.5 \pm 0.1$ MHz and $\gamma_m/2\pi = 1.3 \pm 0.3$ MHz, with error bars corresponding to 95% confidence intervals. The avoided crossing calculated with Eq. (S4) and the parameters determined from the above fits is shown in Fig. S3D.

section S3. QUBIT SPECTRUM IN THE DISPERSIVE REGIME

The effective Hamiltonian of a driven qubit-harmonic oscillator system in the dispersive regime is given by

$$\hat{\mathcal{H}}/\hbar = \frac{1}{2}\Delta_s\hat{\sigma}_z + (\Delta_d + \chi)\,\hat{d}^\dagger\hat{d} + \chi\hat{\sigma}_z\hat{d}^\dagger\hat{d} + \Omega_s\left(\hat{\sigma}^- + \hat{\sigma}^+\right) + \Omega_d\left(\hat{d} + \hat{d}^\dagger\right) \tag{S5}$$

where $\Delta_s = \omega_q - \omega_s$ is the spectroscopy detuning, ω_q is the qubit frequency with the oscillator in the vacuum state, ω_s is the spectroscopy excitation frequency, $\Delta_d = \omega_o^g - \omega_d$ is the drive detuning, $\omega_o^{g(e)}$ is the oscillator frequency with

the qubit in the ground (excited state), $\omega_{\rm d}$ is the drive frequency, $\hat{d}^\dagger$ (d) is the creation (annihilation) operator of the oscillator, χ is the dispersive shift, $\Omega_{\rm s}$ is the spectroscopy excitation strength (Rabi frequency), and $\Omega_{\rm d}$ is the oscillator excitation strength.

From the Hamiltonian of Eq. (S5), Gambetta *et al.* obtained an analytical expression for the qubit spectrum $S(\omega_{\rm s})$ [17], given by

$$S(\omega_{\rm s}) = \sum_{n=0}^{\infty} \frac{1}{\pi}\frac{1}{n!}\mathrm{Re}\left(\frac{(-A)^n e^A}{\gamma_{\rm q}^{(n)} - i\left(\omega_{\rm s} - \tilde{\omega}_{\rm q}^{(n)}\right)}\right) \equiv \sum_{n=0}^{\infty} S_n(\omega_{\rm s}) \tag{S6}$$

with

$$\omega_{\rm q}^{(n)} = \omega_{\rm q} + B + 2\chi n \tag{S7}$$

$$\tilde{\omega}_{\rm q}^{(n)} = \omega_{\rm q}^{(n)} + n\Delta_{\rm d} \tag{S8}$$

$$\gamma_{\rm q}^{(n)} = \gamma_{\rm q} + \kappa\left(n + D^{\rm ss}\right) \tag{S9}$$

$$A = D^{\rm ss}\left(\frac{\kappa/2 - i\left(2\chi + \Delta_{\rm d}\right)}{\kappa/2 + i\left(2\chi + \Delta_{\rm d}\right)}\right) \tag{S10}$$

$$B = \chi(\overline{n}^g + \overline{n}^e - D^{\rm ss}) \tag{S11}$$

$$D^{\rm ss} = \frac{2(\overline{n}^g + \overline{n}^e)\chi^2}{(\kappa/2)^2 + \chi^2 + (\chi + \Delta_{\rm d})^2} \tag{S12}$$

$$\overline{n}^g = \frac{\Omega_{\rm d}^2}{(\kappa/2)^2 + \Delta_{\rm d}^2} \tag{S13}$$

$$\overline{n}^e = \frac{\Omega_{\rm d}^2}{(\kappa/2)^2 + (\Delta_{\rm d} + 2\chi)^2} \tag{S14}$$

In the above equations, $\omega_{\rm q}^{(n)}$ and $\gamma_{\rm q}^{(n)}$ are respectively the frequency and the linewidth of the qubit with the oscillator in the number state $|n\rangle$, $\gamma_{\rm q}$ is the qubit linewidth with the oscillator in the vacuum state, and κ is the linewidth of the harmonic oscillator. The qubit frequency $\omega_{\rm q}^{(0)}$ is ac Stark shifted by B from $\omega_{\rm q}$ and the frequencies $\tilde{\omega}_{\rm q}^{(n)}$ appearing in the spectrum of Eq. (S6) are furthermore shifted by $n\Delta_{\rm d}$ from $\omega_{\rm q}^{(n)}$ (Fig. S1C).

The steady-state distinguishability $D^{\rm ss}$ is defined as the separation between the steady-state coherent states $|\alpha_{g,e}^{\rm ss}\rangle$ created in the oscillator by the microwave excitation with the qubit in the ground state and the excited state, $D^{\rm ss} = \left|\alpha_e^{\rm ss} - \alpha_g^{\rm ss}\right|^2$. The last term in Eq. (S9) shows that as the coherent states $|\alpha_{g,e}^{\rm ss}\rangle$ become more distinguishable, the qubit linewidth $\gamma_{\rm q}^{(n)}$ increases due to the measurement-induced dephasing [17]. The occupancy with the qubit in the ground (excited) state is given by $\overline{n}^{g(e)} = |\alpha_{g(e)}^{\rm ss}|^2 = \langle\hat{n}\hat{\Pi}_{\rm q}^{g(e)}\rangle$, where $\hat{\Pi}_{\rm q}^{g(e)} = |g(e)\rangle\langle g(e)|$ is the projector of the qubit to its ground (excited) state.

For $\chi \gg \kappa$ and $\Delta_{\rm d} = 0$, the steady-state distinguishability $D^{\rm ss}$ is simply given by $D^{\rm ss} = \overline{n}^g + \overline{n}^e$, $A \to -D^{\rm ss}$ and $B \to 0$. In that case, the component of the qubit spectrum with n excitations, $S_n(\omega_{\rm s})$, has a Lorentzian lineshape. The qubit spectrum $S(\omega_{\rm s})$ is therefore well described by a sum of Lorentzian functions at frequencies $\omega_{\rm q}^{(n)}$ and of linewidths $\gamma_{\rm q}^{(n)}$ with a Poisson distributed spectral weight of mean given by $D^{\rm ss}$. However, for $\chi \sim \kappa$, A becomes complex, leading to a non-Lorentzian lineshape for $S_n(\omega_{\rm s})$, with possibly negative values. However, the integral over $\omega_{\rm s}$ of the spectrum and its components is positive in all cases.

section S4. QUBIT SPECTROSCOPY — MAGNON VACUUM STATE

A. Measurement

We perform spectroscopy of the qubit by probing the change Δr in the reflection coefficient r of a readout microwave excitation of fixed frequency ω_r as a function of the spectroscopy frequency ω_s. For all qubit spectroscopy measurements presented here, ω_r is fixed at the frequency of the dressed TE_{103} cavity mode (probe mode) with the qubit in the ground state at $\omega_\mathrm{p}^g/2\pi = 10.44916$ GHz such that $\Delta_\mathrm{r} = \omega_\mathrm{p}^g - \omega_\mathrm{r} = 0$. The readout excitation power P_r is fixed to 9.2 aW, corresponding to an average number of photons in the probe mode much smaller than one. Indeed, the occupancy of the probe mode from the readout excitation is given by

$$\overline{n}_\mathrm{p}^g = \frac{P_\mathrm{r}}{\hbar\omega_\mathrm{p}^g}\frac{\kappa_\mathrm{p}^\mathrm{cpl}}{(\kappa_\mathrm{p}/2)^2} \tag{S15}$$

where κ_p is the the total linewidth of the probe mode and $\kappa_\mathrm{p}^\mathrm{cpl}$ is the coupling rate of the cavity input-output port to the probe mode. With values of $\kappa_\mathrm{p}^\mathrm{cpl}$ and κ_p given in Tables S3, we obtain $\overline{n}_\mathrm{p}^g = 0.078 \pm 0.004$ for $P_\mathrm{r} = 9.2$ aW.

B. Analytical model

To take into account the finite occupancy of the probe mode for qubit spectra measured with the Kittel mode in the vacuum state ($P_\mathrm{mw} = 0$), we use the analytical spectrum $S(\omega_\mathrm{s})$ of Eq. (S6) by considering the probe cavity mode as the harmonic oscillator through the substitutions

$$\begin{gathered} n, \overline{n}^{g,e}, \kappa \to n_\mathrm{p}, \overline{n}_\mathrm{p}^{g,e}, \kappa_\mathrm{p}, \\ \chi \to \chi_\mathrm{q-p}, \\ \Delta_\mathrm{d}, \Omega_\mathrm{d} \to \Delta_\mathrm{r}, \Omega_\mathrm{r}, \\ A, B, D^\mathrm{ss} \to A_\mathrm{p}, B_\mathrm{p}, D_\mathrm{p}^\mathrm{ss} \end{gathered}$$

in Eqs. (S7) to (S14). This leads to

$$S(\omega_\mathrm{s}) = \sum_{n_\mathrm{p}=0}^{\infty} \frac{1}{\pi}\frac{1}{n_\mathrm{p}!}\mathrm{Re}\left(\frac{(-A_\mathrm{p})^{n_\mathrm{p}} e^{A_\mathrm{p}}}{\gamma_\mathrm{q}^{(n_\mathrm{p})} - i\left(\omega_\mathrm{s} - \tilde{\omega}_\mathrm{q}^{(n_\mathrm{p})}\right)}\right) \equiv \sum_{n_\mathrm{p}=0}^{\infty} S_{n_\mathrm{p}}(\omega_\mathrm{s}) \tag{S16}$$

More explicitly, we fit the measured spectrum $\mathrm{Re}(\Delta r)$ to

$$\mathrm{Re}(\Delta r) = \mathcal{A}\sum_{n_\mathrm{p}=0}^{10} S_{n_\mathrm{p}}(\omega_\mathrm{s}) + \mathrm{Re}(\Delta r)_\mathrm{off} \tag{S17}$$

where $\mathcal{A}$ is a conversion factor from $S(\omega_\mathrm{s})$ to $\mathrm{Re}(\Delta r)$, and $\mathrm{Re}(\Delta r)_\mathrm{off}$ is an offset of the spectrum from zero. The Fock basis of the probe mode is truncated to $n_\mathrm{p} = 10$. The linewidth κ_p of the probe mode is fixed to the value determined from a fit of the spectrum of the probe mode (Table S3), and the readout detuning Δ_r is zero. The fitting parameters are the qubit frequency with the probe mode in the vacuum state, ω_q, the qubit linewidth $\gamma_\mathrm{q}(P_\mathrm{s})$ broadened by the spectroscopy microwave excitation of power P_s, the qubit-probe mode dispersive shift $\chi_\mathrm{q-p}$, the probe mode occupancy $\overline{n}_\mathrm{p}^g$ with the qubit in the ground state, the conversion factor $\mathcal{A}$, and the offset $\mathrm{Re}(\Delta r)_\mathrm{off}$.

C. Fit

The measurements and the fits of the qubit spectra for spectroscopy excitation powers P_s of 19 aW and 190 aW are shown in Figs. S4A and S4B. The dispersive shift $\chi_\mathrm{q-p}$ between the qubit and the probe mode is found to be -0.8 ± 0.2 MHz, in excellent agreement with the expected value of -0.73 MHz (Table S2). The power-broadened qubit linewidth $\gamma_\mathrm{q}(P_\mathrm{s})$, shown in Fig. S4C, is fitted to

$$\gamma_\mathrm{q}(P_\mathrm{s}) = \sqrt{\eta P_\mathrm{s} + \gamma_\mathrm{q}(0)^2} \tag{S18}$$

where $\eta \equiv (2\Omega_s)^2/P_s$ relates P_s to the Rabi frequency Ω_s, and $\gamma_q(0)$ is the intrinsic qubit linewidth [27]. The Rabi frequency Ω_s in Eq. (S5) is estimated from the power-broadened qubit linewidth with

$$\Omega_s = \frac{1}{2}\sqrt{\gamma_q(P_s)^2 - \gamma_q(0)^2} \tag{S19}$$

From the fit of $\gamma_q(P_s)$ to Eq. (S18), we find $\gamma_q(0)/2\pi = 0.25^{+0.07}_{-0.10}$ MHz. To obtain this value, we restrict the minimal value of $\gamma_q(P_s)$ in the fit such that the intrinsic linewidth respects the T_1 limit set by $\min[\gamma_q(0)] = 1/T_1$, with $T_1 = 0.63 \pm 0.07$ μs determined in a time-domain measurement. The linewidth $\gamma_q^{(n_p=0)}(0) = \gamma_q(0) + \kappa_p D_p^{ss}$ in Eq. (S9), corresponding to the linewidth of the peak with zero photons and broadened through measurement-induced dephasing from the photon occupancy of the probe mode, is 0.57 ± 0.02 MHz. The difference between $\gamma_q(0)$ and $\gamma_q^{(n_p=0)}(0)$ can be explained by an occupancy in the probe mode of $0.20^{+0.20}_{-0.09}$, significantly higher than the expected occupancy from the probe microwave excitation of 0.078 ± 0.004 previously estimated. This indicates a residual occupancy of $0.12^{+0.21}_{-0.10}$, which should result in a linewidth of $0.44^{+0.54}_{-0.27}$ MHz, broadened from the intrinsic linewidth even in the absence of both probe and spectroscopy microwave excitations. This linewidth compares well with the linewidth of 0.51 ± 0.04 MHz calculated with the dephasing time $T_2^* = 0.62 \pm 0.04$ μs determined from Ramsey interferometry in a time-domain measurement (Figs. S4D and S4E). While all microwave excitations are turned off during the free evolution in the Ramsey interferometry measurement, the residual occupancy of the probe cavity mode creates measurement-induced dephasing of the qubit, increasing the linewidth from 0.25 to 0.51 MHz.

section S5. QUBIT SPECTROSCOPY — MAGNON COHERENT STATE

A. Analytical model and fit

To fit the spectrum of the transmon qubit measured in the dispersive regime with a coherent excitation applied to the Kittel mode ($P_{mw} > 0$), we use the analytical spectrum $S(\omega_s)$ of Eq. (S6) by considering the Kittel mode as the harmonic oscillator through the substitutions

$$\begin{gathered} n, \overline{n}^{g,e}, \kappa \to n_m, \overline{n}_m^{g,e}, \gamma_m, \\ \chi \to \chi_{q-m}, \\ \Delta_d, \Omega_d \to \Delta_{mw}, \Omega_{mw}, \\ A, B, D^{ss} \to A_m, B_m, D_m^{ss} \end{gathered}$$

in Eqs. (S7) to (S14). To take into account the ac Stark shift of the qubit frequency by the photons in the probe mode, we substitute

$$\omega_q \to \omega_q^{(n_p=0)} = \omega_q + B_p \tag{S20}$$

where the ac Stark shifted qubit frequency with the Kittel mode in the vacuum state, $\omega_q^{(n_p=0)}/2\pi = 7.99156$ GHz, is determined from the fit presented in Fig. S4A. The qubit linewidth with the Kittel mode in the vacuum state is substituted to

$$\gamma_q \to \gamma_q^{(n_p=0)} = \gamma_q + \kappa_p D_p^{ss} \tag{S21}$$

to take into account the increase in the linewidth by measurement-induced dephasing from photons in the probe mode, with $\gamma_q^{(n_p=0)}/2\pi = 0.78$ MHz (Fig. S4C and Table S4). With theses substitutions, we fit the qubit spectrum to

$$\mathrm{Re}(\Delta r) = \mathcal{A} \sum_{n_m=0}^{10} S_{n_m}(\omega_s) + \mathrm{Re}(\Delta r)_{off} \tag{S22}$$

where, to take into account the asymmetry in the qubit lineshape from the qubit-probe mode dispersive interaction, we consider the one-photon peak of the probe mode with

$$S_{n_m}(\omega_s) \approx S_{n_m,n_p=0}(\omega_s) + \mathcal{B} \times S_{n_m,n_p=1}(\omega_s) \tag{S23}$$

in Eq. (S22), where

$$\mathcal{B} \equiv \frac{p_{n_p=1}}{p_{n_p=0}} \approx \int d\omega_s \, \frac{S_{n_p=1}(\omega_s)}{S_{n_p=0}(\omega_s)}$$

is the relative spectral weight between the one-photon and the zero-photon peaks. From measurements at $P_{\rm mw} = 0$ (Fig. S4a), we find $\mathcal{B} = 0.03$, which is supposed to be constant in the following analysis. Figure S5A shows an example of the qubit spectrum for a Kittel mode excitation power of 3.1 fW.

The parameters fixed in the fit of the qubit spectrum are the qubit frequency $\omega_{\rm q}^{(n_{\rm p}=0)}$, the power-broadened qubit linewidth $\gamma_{\rm q}^{(n_{\rm p}=0)}$, the magnon linewidth $\gamma_{\rm m}$, the relative spectral weight $\mathcal{B}$, the qubit-probe mode dispersive shift $\chi_{\rm q-p}$, and total linewidth $\kappa_{\rm p}$ of the probe mode. For each Kittel mode excitation power, the fitting parameters are the qubit-magnon dispersive shift $\chi_{\rm q-m}$, the Kittel mode excitation detuning $\Delta_{\rm mw}$, the magnon occupancy with the qubit in the ground state, $\overline{n}_{\rm m}^{g}$ (Fig. 4A in the main text), the conversion factor $\mathcal{A}$, and the offset $\mathrm{Re}(\Delta r)_{\rm off}$ (Fig. S5C). Excitation-power-averaged values of $\Delta_{\rm mw}$ and $\chi_{\rm q-m}$, given in Tables S4 and S2 respectively, are discussed in the main text. Figure S5B shows the splitting between qubit peaks corresponding to successive magnon number states, $2\chi_{\rm q-m} + \Delta_{\rm mw}$, as a function of the Kittel mode excitation power $P_{\rm mw}$. Within error bars, the splitting does not depends on $P_{\rm mw}$.

From the value of $\Delta_{\rm mw}/2\pi = -0.38$ MHz, we can estimate the dressed magnon frequency $\omega_{\rm m}^{g}/2\pi = (\omega_{\rm mw} + \Delta_{\rm mw})/2\pi = 7.94962$ GHz. The Lamb shift $(\omega_{\rm m}^{\rm bare} - \omega_{\rm m}^{g})/2\pi = 1.88$ MHz is calculated from diagonalization of the total Hamiltonian $\hat{\mathcal{H}}$ of Eq. (S1) using parameters of Table S1. This gives a bare magnon frequency $\omega_{\rm m}^{\rm bare}/2\pi = 7.95150$ GHz, from which we calculate $\left|\omega_{\rm q}^{\rm bare} - \omega_{\rm m}^{\rm bare}\right|/2\pi = 89$ MHz, much greater than the qubit-magnon coupling strength of 7.79 MHz.

The offset $\mathrm{Re}(\Delta r)_{\rm off}$ shows a linear scaling with $P_{\rm mw}$, with $\mathrm{Re}(\Delta r)_{\rm off}$ set to zero for $P_{\rm mw} = 0$. The offset appears as a displacement of the reflection coefficient Δr in phase space, indicating an ac Stark shift of the resonant frequency of the probe mode by the occupancy of the Kittel mode. In the detuning-dependent measurement shown in Fig. 2B of the main text, the Kittel mode spectrum is indeed visible through the dispersive interaction between the probe cavity mode and the Kittel mode [32].

B. Kittel mode excitation

In Fig. 4A of the main text, the magnon occupancy $\overline{n}_{\rm m}^{g}$ increases as a function of the Kittel mode excitation power at a rate of 0.342 ± 0.008 magnons per femtowatt. Theoretically, the magnon occupancy $\overline{n}_{\rm m}^{g}$ is given by

$$\overline{n}_{\rm m}^{g} = \frac{\Omega_{\rm mw}^2}{(\gamma_{\rm m}/2)^2 + \Delta_{\rm mw}^2} \tag{S24}$$

with the Kittel mode excitation strength $\Omega_{\rm mw}$ given from the input-output theory by

$$\Omega_{\rm mw} = \sqrt{\frac{P_{\rm mw}}{\hbar\omega_{\rm mw}}} \sum_p \sqrt{\kappa_{10p}^{\rm cpl}} \left[\frac{g_{{\rm m},10p}}{\Delta_{{\rm m},10p}} + \frac{g_{\rm q-m} g_{{\rm q},10p}}{\Delta_{\rm q-m}\sqrt{\Delta_{{\rm m},10p}^2 + \kappa_{10p}^2}} \right] \tag{S25}$$

where $\Delta_{{\rm m},10p} = \omega_{10p}^{\rm bare} - \omega_{\rm m}^{\rm bare}$, $\Delta_{\rm q-m} = \omega_{\rm q}^{\rm bare} - \omega_{\rm m}^{\rm bare}$, and $\Delta_{\rm mw} = \omega_{\rm m}^{g} - \omega_{\rm mw}$. For a given p, the first term of Eq. (S25) describes the excitation of the Kittel mode through a virtual excitation in the TE_{10p} cavity mode, while the second term describes the excitation of the Kittel mode through a virtual excitation in the qubit excited by a virtual excitation in the TE_{10p} cavity mode. This leads to a slope of the magnon occupancy $\overline{n}_{\rm m}^{g}$ as a function of the excitation power $P_{\rm mw}$ given by

$$\frac{\overline{n}_{\rm m}^{g}}{P_{\rm mw}} = \frac{1}{\hbar\omega_{\rm mw}} \frac{1}{(\gamma_{\rm m}/2)^2 + \Delta_{\rm mw}^2} \left(\sum_p \sqrt{\kappa_{10p}^{\rm cpl}} \left[\frac{g_{{\rm m},10p}}{\Delta_{{\rm m},10p}} + \frac{g_{\rm q-m} g_{{\rm q},10p}}{\Delta_{\rm q-m}\sqrt{\Delta_{{\rm m},10p}^2 + \kappa_{10p}^2}} \right] \right)^2 \tag{S26}$$

Truncating to sum over cavity modes to $p = 3$, we calculate $\overline{n}_{\rm m}^{g}/P_{\rm mw} = 0.16^{+0.12}_{-0.06}$ magnons per femtowatt with parameters given in Tables S1 to S4 and with the linewidth and coupling rate of the TE_{101} cavity mode of $\kappa_{101}/2\pi = 1.39$ MHz and $\kappa_{101}^{\rm cpl}/2\pi = 0.13$ MHz, respectively. Error bars correspond to extremal values within the 95% confidence interval of $\kappa_{102}^{\rm cpl} = \kappa_{\rm c}^{\rm cpl}$, $\kappa_{103}^{\rm cpl} = \kappa_{\rm p}^{\rm cpl}$, $\gamma_{\rm m}$, and $\Delta_{\rm mw}$. The discrepancy between the experimental and theoretical slopes of $\overline{n}_{\rm m}^{g}(P_{\rm s})$ of approximately a factor of two is most likely explained by an underestimation of $\Omega_{\rm mw}$ as not all excitation channels of the Kittel mode are taken into account.

C. Probability distribution

The probability p_{n_m} of the magnon number state $|n_\mathrm{m}\rangle$ is calculated as the relative spectral weight of each component $S_{n_\mathrm{m}}(\omega_\mathrm{s})$ of the fitted spectrum $S(\omega_\mathrm{s})$ with

$$p_{n_\mathrm{m}} \approx \int \mathrm{d}\omega_\mathrm{s} \, \frac{S_{n_\mathrm{m}}(\omega_\mathrm{s})}{S(\omega_\mathrm{s})} \tag{S27}$$

where

$$S(\omega_\mathrm{s}) \approx \sum_{n_\mathrm{m}=0}^{10} S_{n_\mathrm{m}}(\omega_\mathrm{s})$$

with $S_{n_\mathrm{m}}(\omega_\mathrm{s})$ given by Eq. (S23). As discussed in Ref. [17], the probability distributions of Eq. (S27) are to be compared with Poisson distributions of mean D_m^ss given by

$$p_{n_\mathrm{m}} = \frac{(D_\mathrm{m}^\mathrm{ss})^{n_\mathrm{m}} \, e^{-D_\mathrm{m}^\mathrm{ss}}}{n_\mathrm{m}!} \tag{S28}$$

Figure S6 shows the comparison between the Poisson distributions and the probability distributions calculated using Eq. (S27) with experimentally determined parameters, but with different values of the magnon linewidth γ_m and excitation detuning Δ_mw. For $\gamma_\mathrm{m} \ll \chi_\mathrm{q-m}$ ($\gamma_\mathrm{m}/2\pi = 0.1$ MHz, Figs. S6A and S6C), the probability distributions given by Eq. (S27) follow the Poisson distributions, even for a finite excitation detuning Δ_mw of -0.38 MHz [17]. However, for $\gamma_\mathrm{m} \sim \chi_\mathrm{q-m}$ ($\gamma_\mathrm{m}/2\pi = 1.3$ MHz, Figs. S6B and S6D), systematic deviations from the Poisson distribution are observed. In that case, despite being in the strong dispersive regime with $|2\chi_\mathrm{q-m}| > \max[\gamma_\mathrm{q}, \gamma_\mathrm{m}]$, the qubit does not perfectly probe the probability distribution of the Kittel mode. Error bars in Fig. 4B of the main text are calculated by finding the extremal values of p_{n_m} calculated within the 95% confidence intervals of the fitting parameters $\overline{n}_\mathrm{m}^g$, $\chi_\mathrm{q-m}$, and Δ_mw.

section S6. MAGNON KERR NONLINEARITY

Using the Hamiltonian of the hybrid system of Eq. (S1), we calculate the magnon Kerr coefficient K_m as a function of the bare magnon frequency $\omega_\mathrm{m}^\mathrm{bare}$ (Fig. S1E). For $\omega_\mathrm{m}^g/2\pi = (\omega_\mathrm{mw} + \Delta_\mathrm{mw})/2\pi = 7.94962$ GHz at $I = -5.02$ mA, we estimate $K_\mathrm{m}/2\pi = -0.12$ MHz. As this coefficient is much smaller than the magnon linewidth of 1.3 MHz, it is not expected to significantly affect the dynamics of the Kittel mode.

However, to understand the effect of this nonzero Kerr coefficient on the behaviour of the magnon occupancy when increasing the Kittel mode excitation power, we consider the effective Hamiltonian of the driven qubit-magnon system in the dispersive regime given by

$$\begin{aligned} \hat{\mathcal{H}}_\mathrm{q-m}/\hbar = &\frac{1}{2}\Delta_\mathrm{s}\hat{\sigma}_z + (\Delta_\mathrm{mw} + \chi_\mathrm{q-m} + K_\mathrm{m}/2)\,\hat{c}^\dagger\hat{c} \\ &+ \chi_\mathrm{q-m}\hat{\sigma}_z\hat{c}^\dagger\hat{c} - (K_\mathrm{m}/2)\left(\hat{c}^\dagger\hat{c}\right)^2 \\ &+ \Omega_\mathrm{s}\left(\hat{\sigma}^- + \hat{\sigma}^+\right) + \Omega_\mathrm{mw}\left(\hat{c} + \hat{c}^\dagger\right) \end{aligned} \tag{S29}$$

where $\Delta_\mathrm{s} = \omega_\mathrm{q} - \omega_\mathrm{s}$ is the spectroscopy detuning, $\Delta_\mathrm{mw} = \omega_\mathrm{m}^g - \omega_\mathrm{mw}$ is the Kittel mode excitation detuning, K_m is the coefficient of the magnon Kerr nonlinearity, Ω_s is the spectroscopy excitation strength (Rabi frequency), and Ω_mw is the Kittel mode excitation strength.

By projecting $\hat{\mathcal{H}}_\mathrm{q-m}$ of Eq. (S29) into the $\hat{\sigma}_z \to -1$ subspace (qubit in the ground state), we obtain the Hamiltonian of a driven Kittel mode with a Kerr nonlinearity

$$\hat{\mathcal{H}}_\mathrm{m}/\hbar = (\Delta_\mathrm{mw} + K_\mathrm{m}/2)\,\hat{c}^\dagger\hat{c} - (K_\mathrm{m}/2)\left(\hat{c}^\dagger\hat{c}\right)^2 + \Omega_\mathrm{mw}\left(\hat{c} + \hat{c}^\dagger\right) \tag{S30}$$

Using Qutip [33,34], we numerically calculate the steady-state magnon occupancy $\overline{n}_\mathrm{m}^g$ with this Hamiltonian and under magnon relaxation at a rate $\gamma_\mathrm{m}/2\pi = 1.3$ MHz, as a function of the Kittel mode excitation strength Ω_mw. The Kittel mode excitation detuning Δ_mw is fixed to zero and -0.38 MHz in Figs. S7A and S7B, respectively. At zero detuning ($\Delta_\mathrm{mw} = 0$), a nonzero Kerr coefficient leads to negative curvature in $\overline{n}_\mathrm{m}^g(\Omega_\mathrm{mw}^2)$ as the excitation gets less efficient when the excitation strength increases, as the increasing magnon occupancy effectively change the excitation

detuning for $|K_\mathrm{m}| > 0$. However, for a finite detuning of -0.38 MHz, the curvature is positive at small $\overline{n}^g_\mathrm{m}$ for a finite range of Kerr coefficients $K_\mathrm{m} < 0$. Indeed, in this case, the Kerr nonlinearity compensate the finite detuning, making the Kittel mode excitation more efficient as the magnon occupancy increases. For larger values of $\overline{n}^g_\mathrm{m}$, the curvature becomes negative, as shown in the inset of Fig. S7B.

We now compare the numerically calculated $\overline{n}^g_\mathrm{m}(\Omega^2_\mathrm{mw})$ to the data $\overline{n}^g_\mathrm{m}(P_\mathrm{mw})$ of Fig. 4A in the main text. Figures S7C and S7D shows the coefficient of determination R^2 between $\overline{n}^g_\mathrm{m}(\Omega^2_\mathrm{mw})$ and $\overline{n}^g_\mathrm{m}(P_\mathrm{mw})$ for different values of the Kerr coefficient K_m and the proportionally constant between Ω^2_mw and P_mw. Maximizing the coefficient of determination R^2, we determine a Kerr coefficient K_m of $-0.20^{+0.05}_{-0.14}$ MHz for $\Delta_\mathrm{mw}/2\pi = -0.38$ MHz. Error bars on K_m are calculated by finding the extremal values found within the 95% confidence interval of γ_m and Δ_mw. Even if the magnon Kerr coefficient is much smaller than the magnon linewidth, the value found from the fit is in relatively good agreement with the value of -0.12 MHz in Fig. S1D.

Figure S8 shows that deviations from Poisson distributions in the magnon probability distributions expected from the finite Kerr nonlinearity are much smaller than deviations expected from the estimation of the probability distributions with Eq. (S27).

Finally, no thermal occupancy of the Kittel mode is found within our error bars of about 0.01 magnons, indicating an effective magnon temperature smaller than ~ 80 mK.

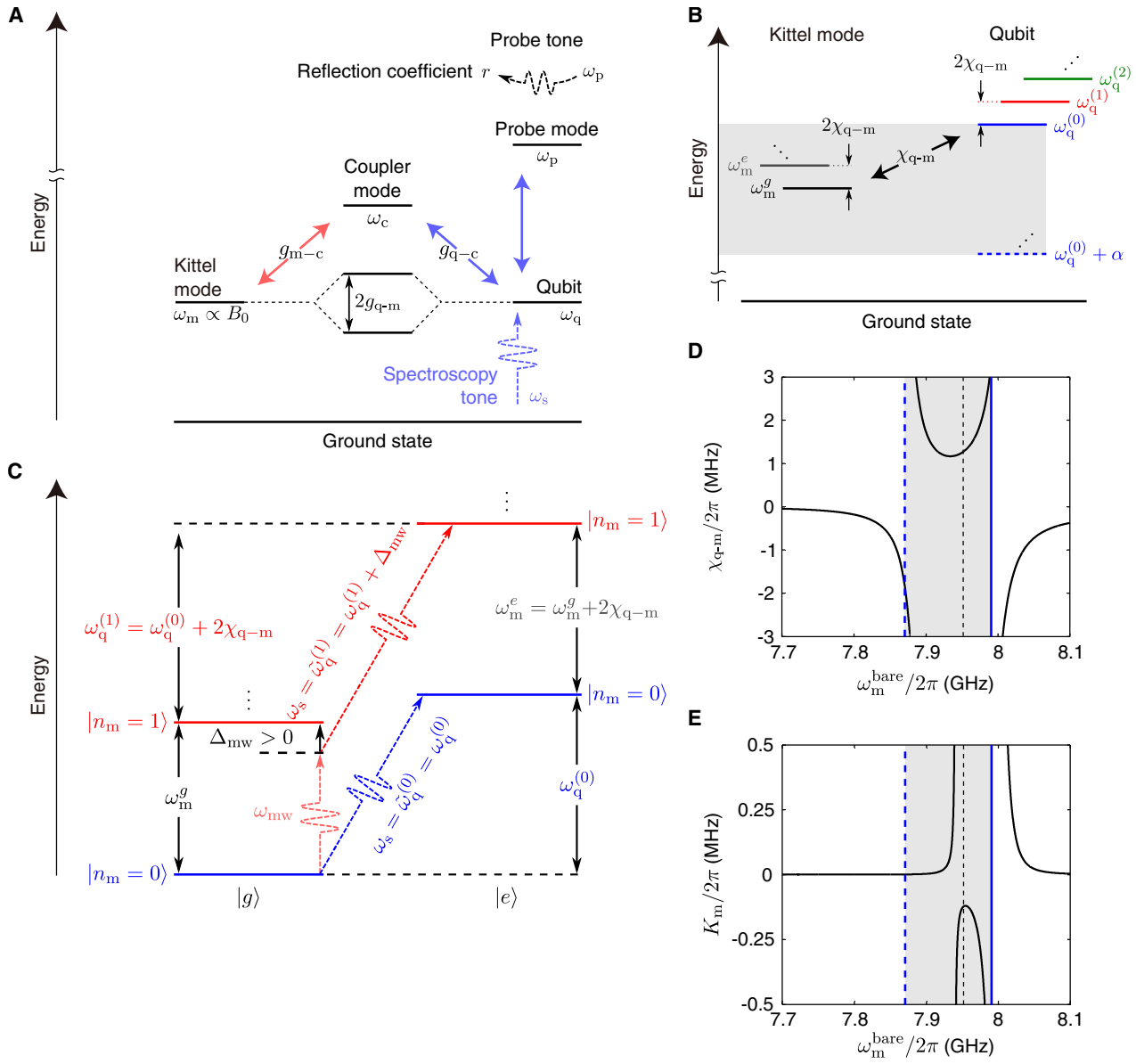

fig. S1. Qubit-magnon hybrid system. **(A)** Schematic energy diagram of the coupler and probe cavity modes, the qubit, and the Kittel mode, respectively of frequencies ω_c, ω_p, ω_q, and ω_m. The qubit and the Kittel mode are coupled to the coupler cavity mode through electric and magnetic dipole interactions, at rates g_{q-c} and g_{m-c}, respectively. The spectrum of the qubit is measured by probing reflection of a microwave excitation of frequency ω_r resonant with the frequency of the probe mode with the qubit in the ground state, ω_p^g, as a function of the spectroscopy frequency ω_s. **(B)** Schematic energy diagram for the qubit and the Kittel mode in the dispersive regime, indicating the transitions $|g\rangle \leftrightarrow |e\rangle$ and $|e\rangle \leftrightarrow |f\rangle$ of the transmon at frequencies $\omega_q^{(n_m)}$ and $\omega_q^{(n_m)} + \alpha$ respectively, where $\alpha(< 0)$ is the transmon anharmonicity and $|n_m = \{0, 1, 2, \dots\}\rangle$ are the magnon number states. The straddling regime corresponds to $\omega_q^{(0)} + \alpha < \omega_m^g < \omega_q^{(0)}$ (shaded area), where $\omega_m^{g(e)}$ is the magnon frequency with the qubit in the ground (excited) state $|g(e)\rangle$. **(C)** A microwave excitation at ω_{mw} is used to drive the Kittel mode at a detuning $\Delta_{mw} = \omega_m^g - \omega_{mw}$, leading to peaks in the qubit spectrum at frequencies $\tilde{\omega}_q^{(n_m)} = \omega_q^{(n_m)} + n_m \Delta_{mw}$. The splitting between peaks corresponding to successive magnon number states is therefore given by $2\chi_{q-m} + \Delta_{mw}$. Calculation of **(D)** the qubit-magnon dispersive shift χ_{q-m} and **(E)** the magnon Kerr coefficient K_m as a function of the bare magnon frequency ω_m^{bare} using the parameters of Table S1. The straddling regime (shaded area) corresponds to ω_m^{bare} between the transmon $|g\rangle \leftrightarrow |e\rangle$ transition frequency (ω_q, blue solid lines) and $|e\rangle \leftrightarrow |f\rangle$ transition frequency ($\omega_q + \alpha$, blue dashed lines, where $\alpha(< 0)$ is the transmon anharmonicity) with the Kittel mode in the vacuum state. Vertical black dashed line show $\omega_m^{bare}/2\pi = 7.95150$ GHz, calculated from the experimentally determined $\omega_m^g/2\pi = 7.94962$ GHz and the calculated Lamb shift $(\omega_m^{bare} - \omega_m^g)/2\pi = 1.88$ MHz.

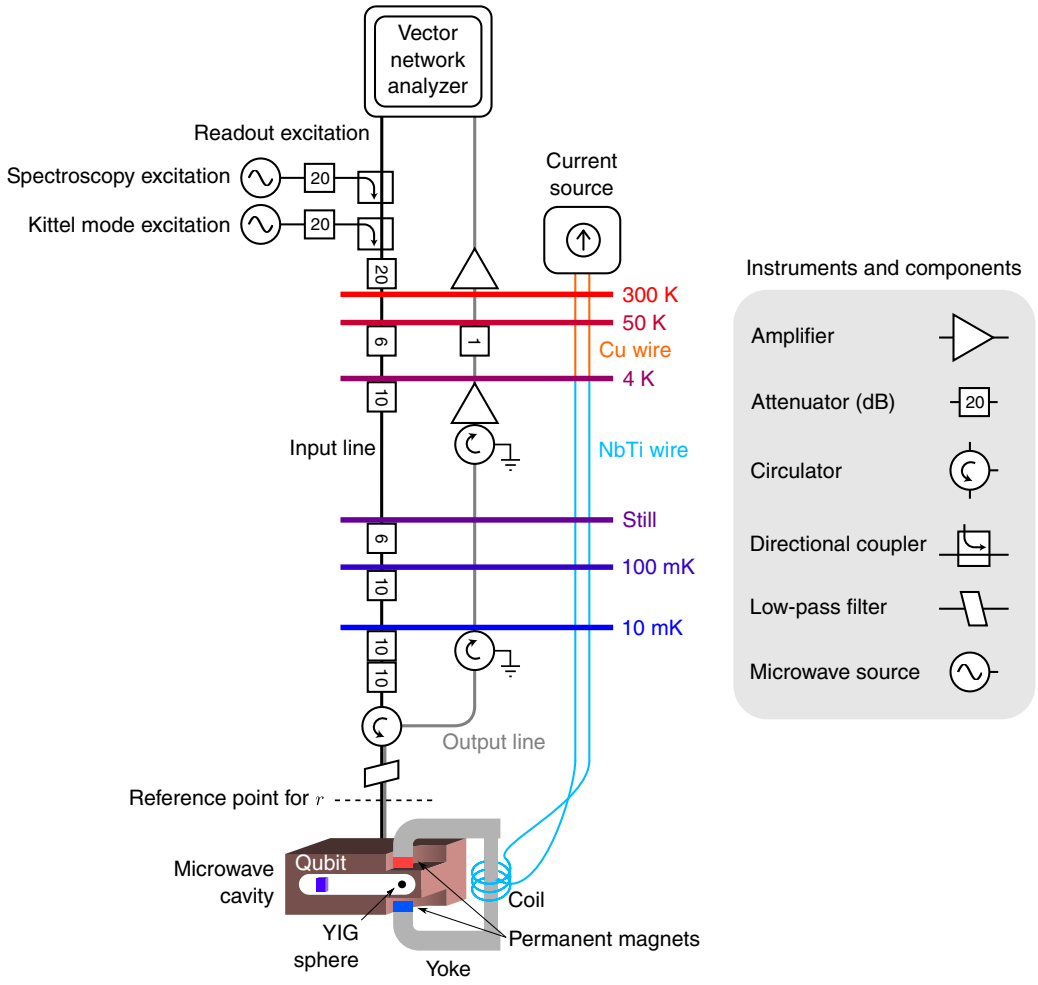

fig. S2. Experimental setup. Spectroscopic measurements are performed with a vector network analyzer (Agilent E5071C). The microwave excitations are generated by microwave sources (Agilent E8247C), combined with the readout microwave excitation from the vector network analyzer in directional couplers (Krytar 120420), and introduced to the input port of the dilution refrigerator. The reflected signal from the cavity is amplified by amplifiers at 4 K (Caltech CRYO4-12) and at room temperature (MITEQ AFS4-08001200-09-10P-4). A current source (Yokogawa GS200) is used to supply the current I to the coil through Cu wires (orange) and superconducting NbTi wires (pale blue). The attenuation of the input line (black) in the dilution refrigerator, of about 59 dB at 10 GHz including losses in cables (phosphor-bronze coaxial cables; Coax Corp. SC-119/50-PBC-PBC) and connectors, is to prevent room-temperature thermal noise from reaching the hybrid system. A low-pass filter at 12 GHz (RLC F-30-12.4-R) is used to further decrease noise into the cavity. Noise from the room-temperature environment and the amplifiers in the output line (grey) are attenuated by more than 60 dB by a circulator (Quinstar XTE0812KCS) and two isolators (Quinstar XTE0812KCS and XTE0812KC). A superconducting NbTi coaxial cable is used in the output line between the two isolators.

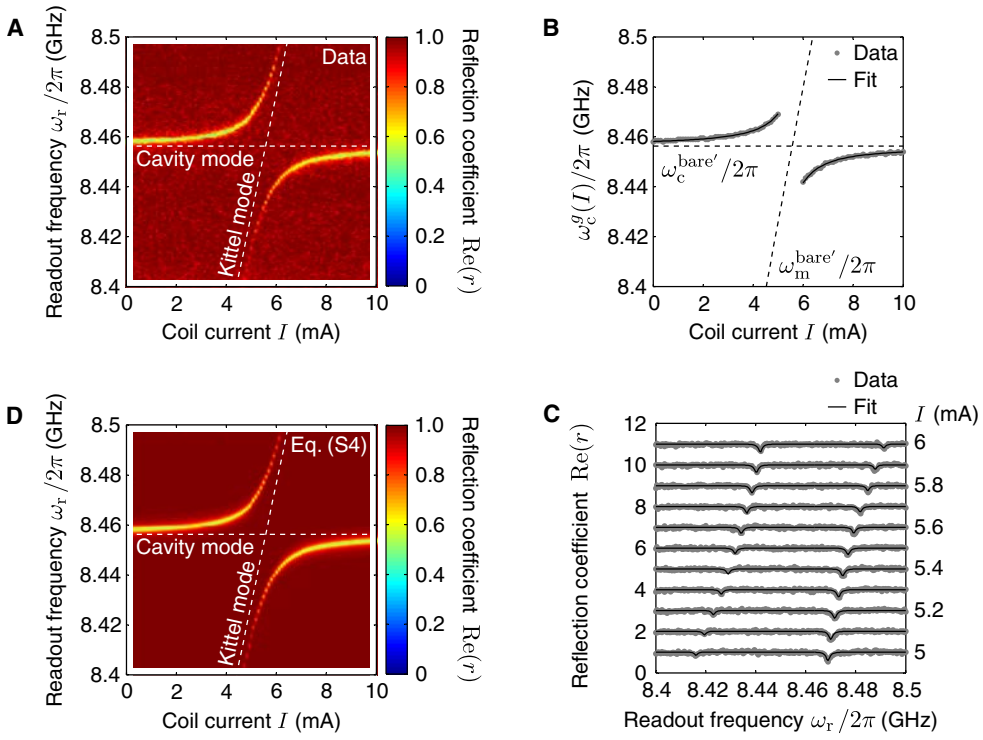

fig. S3. Cavity-magnon coupling. **(A)** Measurement of the reflection coefficient $\mathrm{Re}(r)$ of a readout microwave excitation at frequency ω_r as a function of the coil current I. Both the spectroscopy and Kittel mode microwave excitations are turned off for this measurement. The avoided crossing in the coupler cavity mode spectrum indicates the coherent interaction between this cavity mode and the Kittel mode. **(B)** Fit of the dressed frequency of the coupler cavity mode with the qubit in the ground state, $\omega_c^g(I)$, to Eq. (S3). **(C)** Fit of the coupler cavity mode spectrum to Eq. (S4) for different coil currents near the avoided crossing ($I = 5$ to 6 mA). Individual spectra are offset vertically by $\mathrm{Re}(r) = 1$ for clarity. **(D)** Coupler cavity mode spectrum as a function of I calculated using Eq. (S4) with $g_{\mathrm{m-c}}/2\pi = 22.5$ MHz and $\gamma_m/2\pi = 1.3$ MHz. For **(A)**, **(B)** and **(D)**, coupler and Kittel modes frequencies bare of their mutual interaction, $\omega_c^{\mathrm{bare}'}$ and $\omega_m^{\mathrm{bare}'}$ respectively, are shown as horizontal and diagonal dashed lines.

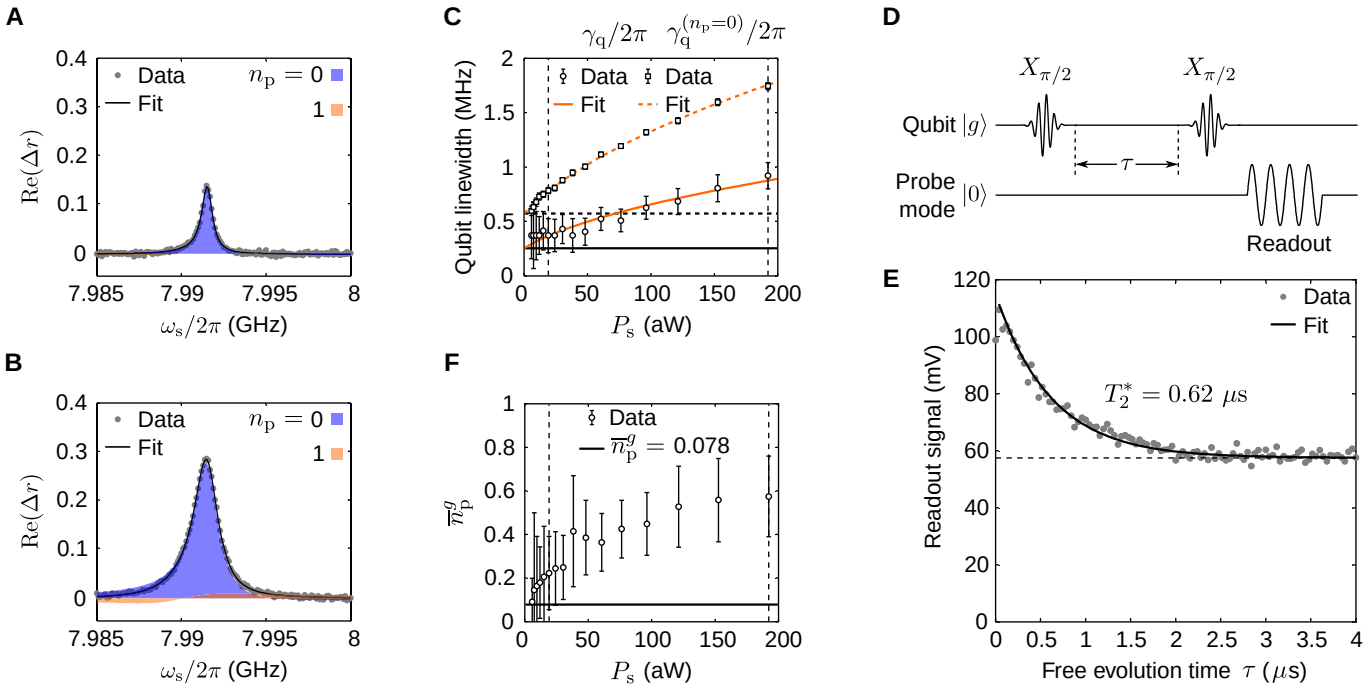

fig. S4. Power broadening of the qubit spectrum. Qubit spectra for spectroscopy excitation powers P_s of **(A)** 19 aW and **(B)** 190 aW. Fits of data to Eq. (S17) are shown as black lines. Blue and orange shaded areas respectively show the peaks corresponding to zero and one photons in the probe cavity mode. Note that the asymmetry in the qubit lineshape is very well reproduced by the fit. **(C)** Power-broadened qubit linewidths γ_q (circles) and $\gamma_\mathrm{q}^{(n_\mathrm{p}=0)}$ (squares) in Eq. (S9) as a function of P_s. Solid and dashed orange lines show fits to Eq. (S18), indicating linewidths $\gamma_\mathrm{q}(0)/2\pi = 0.25$ MHz (horizontal black solid line) and $\gamma_\mathrm{q}^{(n_\mathrm{p}=0)}(0)/2\pi = 0.57$ MHz (horizontal black dashed line) for $P_\mathrm{s} \to 0$. **(D)** Pulse sequence used to measure the qubit dephasing time T_2^* with Ramsey interferometry. An initial $\pi/2$ pulse prepares the qubit in a coherent superposition between the $|g\rangle$ and $|e\rangle$ states. After a time τ during which the qubit evolves freely, a second $\pi/2$ pulse is applied to the qubit. In the frame rotating at the qubit frequency, these two pulses would ideally result in the qubit in the excited state. In the presence of dephasing, the probability of finding the qubit in the excited state decays on a timescale given by the dephasing time T_2^*. Readout is performed by sending a strong microwave pulse resonant with the probe mode [31]. **(E)** Readout signal as a function of the free evolution time τ between the two $\pi/2$ pulses. From the fit, we extract $T_2^* = 0.62$ μs. The zero of the readout signal is defined as the signal with the qubit in the ground state, such that the readout signal is proportional to the probability p_e of finding the qubit in the excited state after the pulse sequence shown in **(D)**. **(F)** Occupancy of the probe cavity mode as a function of P_s. Horizontal solid line shows the occupancy $\overline{n}_\mathrm{p}^g = 0.078$ calculated with Eq. (S15). For **(C)** and **(F)**, vertical dashed lines show $P_\mathrm{s} = 19$ aW and 190 aW.

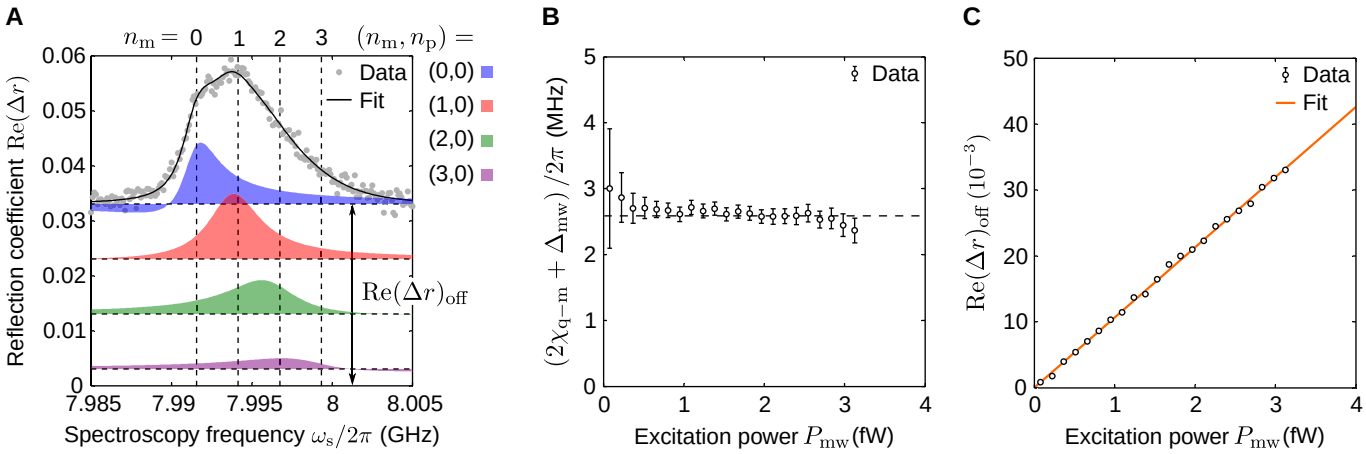

fig. S5. Dispersive qubit-magnon interaction. **(A)** Qubit spectrum for $P_{\mathrm{mw}} = 3.1$ fW and the corresponding fit (black line). Color-coded shaded areas show components of the spectrum corresponding to different magnon number states $|n_{\mathrm{m}}\rangle$ and probe mode in the vacuum state $|n_{\mathrm{p}} = 0\rangle$. Components of the spectrum corresponding to one photon in the probe mode are not clearly visible and are therefore not shown. Components corresponding to $|n_{\mathrm{m}} = \{1, 2, 3\}\rangle$ are offset vertically by -0.01, -0.02 and -0.03, respectively, from the spectrum offset $\mathrm{Re}(\Delta r)_{\mathrm{off}}$. Negative values in the spectrum component corresponding to $n_{\mathrm{m}} = 0$ are visible for $\omega_{\mathrm{s}}/2\pi \lesssim 7.99$ GHz. Vertical dashed lines indicate the frequencies of the qubit $|g\rangle \leftrightarrow |e\rangle$ transitions corresponding to the first four magnon number states neglecting the ac Stark shift $B_{\mathrm{m}}/2\pi = -0.23$ MHz, small relative to the dispersive shift per magnon $2\chi_{\mathrm{q-m}}$ of 3 MHz. **(B)** Splitting between qubit transitions corresponding to successive magnon number states, $2\chi_{\mathrm{q-m}} + \Delta_{\mathrm{mw}}$, as a function of the Kittel mode excitation power P_{mw}. At low excitation powers, it is difficult to determine from the splitting of the peaks the dispersive shift $\chi_{\mathrm{q-m}}$ and the excitation detuning Δ_{mw} independently. We therefore omit data points for $P_{\mathrm{mw}} < 0.9$ fW to estimate average values and standard deviations of $\chi_{\mathrm{q-m}}$ and Δ_{mw}. However, the splitting $2\chi_{\mathrm{q-m}} + \Delta_{\mathrm{mw}}$ is constant (within error bars) at 2.6 ± 0.3 MHz for all excitation powers. **(C)** Offset $\mathrm{Re}(\Delta r)_{\mathrm{off}}$ as a function of the Kittel mode excitation power P_{mw}. The orange solid line shows a linear fit of $\mathrm{Re}(\Delta r)_{\mathrm{off}}$. In **(B)** and **(C)**, error bars indicate 95% confidence intervals. In **(C)**, error bars are smaller than the symbols.

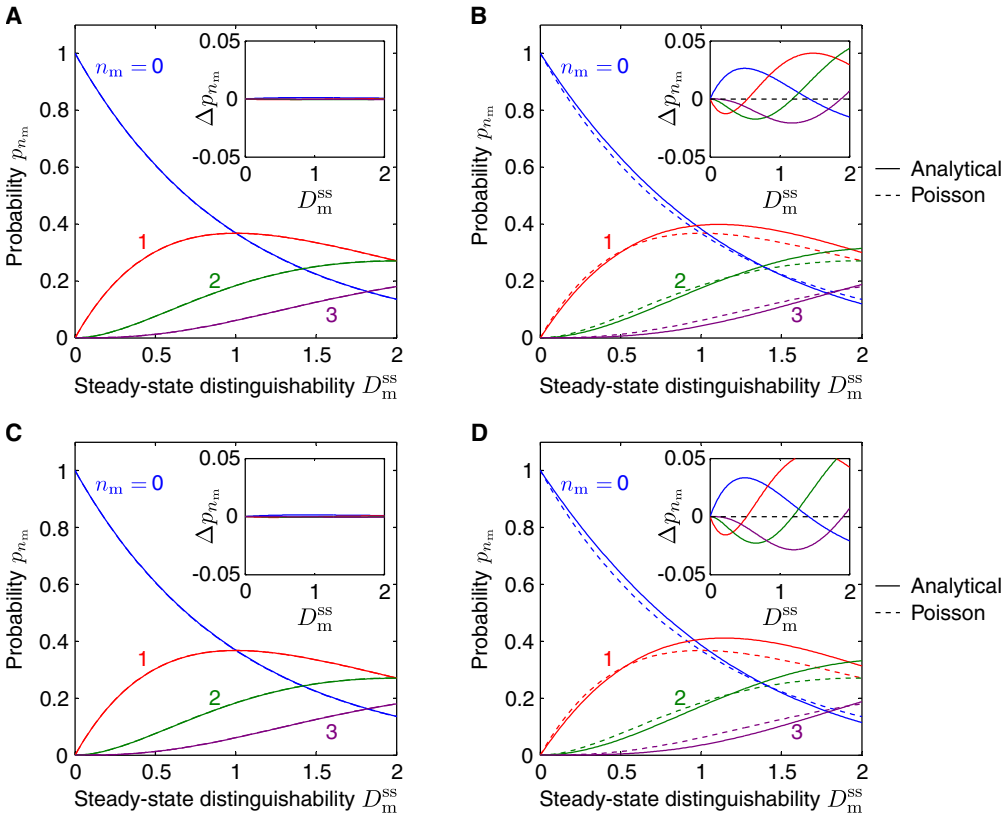

fig. S6. Probability distributions. Probability distributions of magnon number states calculated with Eq. (S27) (solid lines) and Eq. (S28) (Poisson distribution, dashed lines) for **(A)** $\gamma_m/2\pi = 0.1$ MHz and $\Delta_{mw} = 0$, **(B)** $\gamma_m/2\pi = 1.3$ MHz and $\Delta_{mw} = 0$, **(C)** $\gamma_m/2\pi = 0.1$ MHz and $\Delta_{mw}/2\pi = -0.38$ MHz, and **(D)** $\gamma_m/2\pi = 1.3$ MHz and $\Delta_{mw}/2\pi = -0.38$ MHz. Insets show deviations Δp_{n_m} from Poisson distributions.

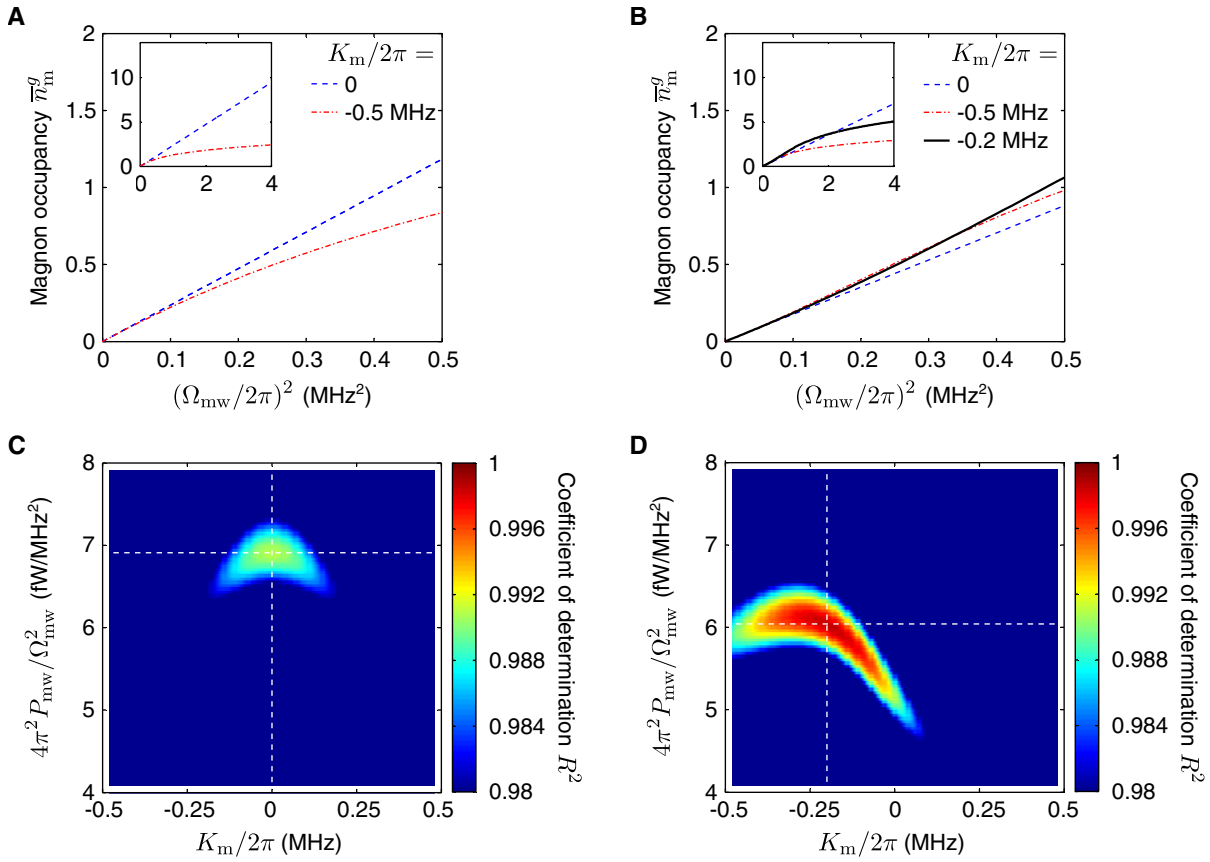

fig. S7. Magnon Kerr nonlinearity. **(A)**, **(B)** Numerical calculation of the magnon occupancy $\overline{n}^g_{\rm m}$ as a function of the Kittel mode excitation power, proportional to $\Omega^2_{\rm mw}$, using the Hamiltonian of Eq. (S30) for different values of $K_{\rm m}$ and with a magnon linewidth $\gamma_{\rm m}$ of 1.3 MHz. The Kittel mode excitation detuning $\Delta_{\rm mw}$ is **(A)** zero and **(B)** -0.38 MHz. Insets shows a larger range of Kittel mode excitation power. **(C)**, **(D)** Coefficient of determination R^2 between $\overline{n}^g_{\rm m}(P_{\rm mw})$ (data, Fig. 4A in the main text) and $\overline{n}^g_{\rm m}(\Omega_{\rm mw})$ (simulations, this figure) as a function of $K_{\rm m}$ and the proportionality constant between $P_{\rm mw}$ and $\Omega^2_{\rm mw}$. The Kittel mode excitation detuning $\Delta_{\rm mw}$ is **(C)** zero and **(D)** -0.38 MHz. Vertical and horizontal dashed lines show best fit values of $K_{\rm m}$ and $4\pi^2 P_{\rm mw}/\Omega^2_{\rm mw}$, respectively.

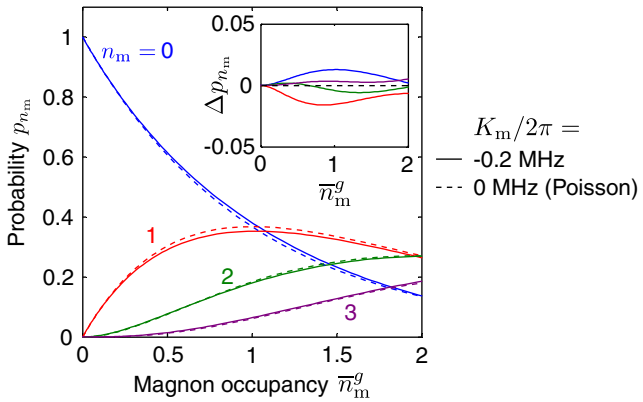

fig. S8. Effect of the finite Kerr nonlinearity on the magnon probability distribution. Probability distributions of magnon number states calculated from the steady-state density matrix obtained by numerically solving the master equation derived from the Hamiltonian of Eq. (S30) and considering magnon relaxation. Parameters: $\gamma_{\rm m}/2\pi = 1.3$ MHz, $\Delta_{\rm mw}/2\pi = -0.38$ MHz, and $K_{\rm m}/2\pi = -0.2$ MHz (solid lines) and $K_{\rm m}/2\pi = 0$ (dashed lines). Inset: deviations $\Delta p_{n_{\rm m}}$ from Poisson distributions.

table S1. Parameters of the hybrid system.

Parameters of the hybrid system used for the calculation of the qubit-magnon coupling strength $g_{\mathrm{q-m}}$, the qubit-probe mode dispersive shift $\chi_{\mathrm{q},103} = \chi_{\mathrm{q-p}}$, the qubit-magnon dispersive shift $\chi_{\mathrm{q-m}}$, and the magnon Kerr coefficient K_{m}. Parameters in parentheses are numerically estimated based on electromagnetic field simulations.

Parameter	Symbol	Value (MHz)
TE_{101} cavity mode bare frequency	$\omega_{101}^{\mathrm{bare}}/2\pi$	6994.0
TE_{102} cavity mode bare frequency	$\omega_{102}^{\mathrm{bare}}/2\pi = \omega_{\mathrm{c}}^{\mathrm{bare}}/2\pi$	8414.5
TE_{103} cavity mode bare frequency	$\omega_{103}^{\mathrm{bare}}/2\pi = \omega_{\mathrm{p}}^{\mathrm{bare}}/2\pi$	$10,441.5$
TE_{104} cavity mode bare frequency	$\omega_{104}^{\mathrm{bare}}/2\pi$	$(12,800)$
Transmon bare $\lvert g\rangle \leftrightarrow \lvert e\rangle$ transition frequency	$\omega_{\mathrm{q}}^{\mathrm{bare}}/2\pi$	8040.6
Transmon bare anharmonicity	$\alpha^{\mathrm{bare}}/2\pi$	-137.2
TE_{101} cavity mode-qubit coupling rate	$g_{\mathrm{q},101}/2\pi$	73
TE_{102} cavity mode-qubit coupling rate	$g_{\mathrm{q},102}/2\pi = g_{\mathrm{q-c}}/2\pi$	126.1
TE_{103} cavity mode-qubit coupling rate	$g_{\mathrm{q},103}/2\pi = g_{\mathrm{q-p}}/2\pi$	135.4
TE_{104} cavity mode-qubit coupling rate	$g_{\mathrm{q},104}/2\pi$	(116)
TE_{101} cavity mode-Kittel mode coupling rate	$g_{\mathrm{m},101}/2\pi$	(-13.6)
TE_{102} cavity mode-Kittel mode coupling rate	$g_{\mathrm{m},102}/2\pi = g_{\mathrm{m-c}}/2\pi$	22.5
TE_{103} cavity mode-Kittel mode coupling rate	$g_{\mathrm{m},103}/2\pi = g_{\mathrm{m-p}}/2\pi$	(-20.3)
TE_{104} cavity mode-Kittel mode coupling rate	$g_{\mathrm{m},104}/2\pi$	(14.0)

table S2. Comparison between experimental and theoretical values.

Comparison between experimental and theoretical values, respectively determined from measurements and from diagonalization of the total Hamiltonian $\hat{\mathcal{H}}$ of Eq. (S1) using parameters of Table S1. The qubit-probe mode dispersive shift $\chi_{\mathrm{q-p}}$, the qubit-magnon dispersive shift $\chi_{\mathrm{q-m}}$, and the magnon Kerr coefficient K_{m} are evaluated at $\omega_{\mathrm{m}}^{\mathrm{bare}}/2\pi = 7.95150$ GHz for $I = -5.02$ mA.

Parameter	Symbol	Value (MHz)		Error (%)	Figure
		Experimental	Theoretical		
Qubit-magnon coupling strength	$g_{\mathrm{q-m}}/2\pi$	7.79	6.67	+17	1
Qubit-probe mode dispersive shift	$\chi_{\mathrm{q-p}}/2\pi$	-0.8 ± 0.2	-0.73	+9	S4
Qubit-magnon dispersive shift	$\chi_{\mathrm{q-m}}/2\pi$	1.5 ± 0.1	1.27	+18	2 to 4, S1D, and S5B
Magnon Kerr coefficient	$K_{\mathrm{m}}/2\pi$	$-0.20^{+0.09}_{-0.13}$	-0.12	+58	S1E

table S3. Linewidths of the hybrid system. Figures in Supplementary Information related to the parameters are indicated when available. Error bars indicate 95% confidence intervals.

Parameter	Symbol	Value (MHz)	Figure
Coupler cavity mode linewidth	$\kappa_{\mathrm{c}}/2\pi$	2.08 ± 0.02	-
Coupler cavity mode internal loss rate	$\kappa_{\mathrm{c}}^{\mathrm{int}}/2\pi$	1.58 ± 0.02	-
Coupling rate to the coupler cavity mode	$\kappa_{\mathrm{c}}^{\mathrm{cpl}}/2\pi$	0.51 ± 0.02	-
Probe cavity mode linewidth	$\kappa_{\mathrm{p}}/2\pi$	3.72 ± 0.03	-
Probe cavity mode internal loss rate	$\kappa_{\mathrm{p}}^{\mathrm{int}}/2\pi$	2.45 ± 0.03	-
Coupling rate to the probe cavity mode	$\kappa_{\mathrm{p}}^{\mathrm{cpl}}/2\pi$	1.27 ± 0.03	-
Intrinsic qubit linewidth	$\gamma_{\mathrm{q}}(0)/2\pi$	$0.25^{+0.07}_{-0.10}$	S4C
Kittel mode linewidth	$\gamma_{\mathrm{m}}/2\pi$	1.3 ± 0.3	S3

table S4. Experimental parameters of the measurements.

Experimental parameters of the measurements presented in the figures of the main text. Figures in Supplementary Information related to the parameters are indicated when available. Error bars indicate 95% confidence intervals.

Parameter	Symbol	Value in Fig. 1	Value in Fig. 2	Value in Fig. 3	Figure
Readout excitation power	P_{r}	9.2 aW			-
Readout excitation frequency	$\omega_{\mathrm{r}}/2\pi$	10.44916 GHz			-
Probe mode occupancy	$\overline{n}_{\mathrm{p}}^{g}$	0.6 ± 0.2		0.22 ± 0.17	S4F
Spectroscopy excitation power	P_{s}	190 aW		19 aW	-
Broadened qubit linewidth	$\gamma_{\mathrm{q}}^{(n_{\mathrm{p}}=0)}(P_{\mathrm{s}})/2\pi$	1.74 ± 0.04 MHz		0.78 ± 0.03 MHz	S4C
Kittel mode excitation power	P_{mw}	-	7.9 fW	$[0.079, 3.1]$ fW	-
Kittel mode excitation detuning	$\Delta_{\mathrm{mw}}/2\pi$	-	$[-10.38, 4.62]$ MHz	-0.38 ± 0.08 MHz	S5B